PbSe Nanocrystal Network Formation during Pyridine Ligand Displacement

Tobias Hanrath,[*,†] **Dirk Veldman,**[†] **Joshua J. Choi,**[†] **Christina G. Christova,**[†] **Martijn M. Wienk,**[†] **and René A. J. Janssen**[*,‡]

School of Chemical and Biomolecular Engineering, Cornell University, Ithaca, New York, 14853, and Departments of Applied Physics and Chemical Engineering & Chemistry, Eindhoven University of Technology, P.O. Box 513, 5600 MB Eindhoven, The Netherlands

ABSTRACT Solution-phase pyridine treatment displaced oleic acid capping ligands from the surface of PbSe nanocrystals. During ligand displacement the nanostructure morphology dramatically changed from well-stabilized, individual nanocrystals to form crystallographically connected nanocrystal networks. The network morphology was governed by the diameter of the constituent nanocrystals. Larger nanocrystals showed dipolar alignment but maintained individual nanocrystal character, while smaller nanocrystals crystallographically fused along the ⟨100⟩ axis. Optical studies of nanocrystal thin films showed that pyridine ligand displacement quenches the nanocrystal photoluminescence. Blends of nanocrystals and conjugated polymer showed photoluminescence quenching of the polymer with increasing nanocrystal content. The extent of photoluminescence quenching was only weakly dependent on the nanocrystal size or surface chemistry, suggesting that the interaction between nanocrystal and polymer is mostly in the form of energy transfer rather than charge transfer.

KEYWORDS: semiconductor nanocrystals • surface chemistry • dipole mediated network formation

INTRODUCTION

Currently, the two greatest challenges in applied nanomaterials research are controlling and understanding nanocrystal network morphology and surface chemistry. These aspects are particularly well illustrated in blends of inorganic and organic semiconductors, which have been intensively studied as active layers for inexpensive optoelectronic devices. The synergistic integration of easy processing of polymers and efficient charge transport and photon absorption in inorganic nanocrystals is a particularly attractive option for active layers in future low-cost, high-efficiency photovoltaic devices (1−5).

Among the many semiconductor nanocrystal materials under investigation for photovoltaic applications, PbSe nanocrystals have emerged as one of the most intriguing candidates. Synthetic control over the nanocrystal diameter combined with the large exciton Bohr radius of PbSe (46 nm) (6) permits precise tuning of the quantum confined energy gap in the range of 0.3−1.0 eV—enabling solar energy conversion in the near-infrared (7−11). Moreover, PbSe nanocrystals can be prepared in an impressive array of shapes, including spheres, cubes, wires, stars, and rings (12−14). Most recently, the discovery of highly efficient multiexciton generation (MEG) in PbSe nanocrystals has drawn intense attention from applied and fundamental research communities (15−18). MEG converts a single incident solar photon into multiple electron hole pairs and opens the door toward solar cells with efficiencies surpassing the vexing Shockley−Queisser limit for a single band gap semiconductor (19−21).

To harness the full potential of this material system, three key criteria have to be met: (1) the energy levels of the composite materials have to align complimentarily to facilitate dissociation of photogenerated excitons into charges at the interface, (2) the kinetics of exciton dissociation and charge transport have to be faster than their recombination, and (3) the morphology of the hybrid material has to provide high interface area for exciton dissociation and simultaneously a continuous transport pathway for each charge to their respective external electrode.

Previous studies have shown that these energetic, kinetic, and morphological criteria are highly sensitive to physical and chemical interface properties (1−5). In the case of semiconductor nanocrystals embedded in conjugated polymers, the nanocrystal surface chemistry must be delicately balanced to serve two conflicting roles. On the one hand, the nanocrystals must be shielded from mutual van der Waals attractions to preserve colloidal stability and enable solution processing of the nanocrystal/polymer blend. On the other hand, the nanocrystal surface must be electrically coupled to its surroundings for fast and efficient charge transfer across the nanocrystal boundary. Earlier efforts to mitigate these requirements can be placed into two broad categories. One has focused on covalent attachment of conjugated oligomers to the nanocrystal surface (22). Despite improved miscibility and electrical coupling between the nanocrystal and the hole-conducting polymer, this approach effectively isolated interparticle communication and

hence only solved the separation and transport challenge for one carrier, the hole.

An alternative approach is to partially remove the insulating ligand or to replace it with shorter bifunctional linker molecules (23−25). This treatment has profound influence on electronic interparticle coupling, as manifested in more than 10 orders of magnitude improvement in nanocrystal film conductivity (23). Unfortunately, the enhanced nanocrystal ensemble conductivity is offset by the insolubility of nanocrystal films treated with short linkers. What is needed is a nanostructure assembly that combines miscibility and efficient electrical coupling of nanocrystals with each other and their surrounding environment. In this work, we investigate the displacement of oleic acid ligand from the surface of PbSe nanocrystals in pyridine and illustrate that the treatment is accompanied by dramatic changes in the morphology and the connection of individual nanocrystals into larger, partly ordered structures and networks.

EXPERIMENTAL SECTION

PbSe nanocrystals were prepared following the method reported by Yu et al. (26) and modified by replacing the 1-octadecene solvent with squalene. The synthesis was carried out in a three-necked flask under an inert Ar atmosphere. In a typical synthesis, PbO (1 mmol) and oleic acid (3 mmol) were dissolved in squalene to yield a precursor solution with [Pb] = 0.13 M and a molar Pb to oleic acid ratio of 1:3. The solution was then degassed by heating to 160 °C for 1 h under flowing Ar. In a glovebox, Se was dissolved in trioctylphosphine (TOP) to yield a 1 M stock solution. Three milliliters of the 1 M TOP−Se solution was rapidly injected into the vigorously stirred, hot lead oleate solution. PbSe nanocrystals formed immediately after injection, and their size was tuned through adjustments in temperature (120−180 °C), reaction time (2−5 min), and Pb to oleic acid molar ratio (1:6 to 1:3). After the elapsed reaction time, the solution was quenched by transferring the flask to a water bath. Following synthesis, the nanocrystals were washed several times by sequential precipitation with ethanol and redispersion in anhydrous hexane.

The surface ligand displacement protocol was adopted from literature methods for CdSe nanocrystals (27). Under an inert argon atmosphere, oleate-passivated PbSe nanocrystals were dispersed in pyridine at a concentration of 5−10 mg/mL by a brief ultrasonication and stirred at 60 °C for 3−6 h. Pyridine-treated nanocrystals were precipitated by addition of hexane, isolated by centrifugation, and subsequently redispersed either in pristine pyridine or in mixtures of pyridine and chlorobenzene. TEM samples were prepared by drop-casting diluted nanocrystal solutions onto carbon-coated 300 mesh Cu TEM grids. TEM images were taken on either an FEI Tecnai 20 (type Sphera) operated with a 200 kV LaB6 filament or an FEI Titan equipped with a 300 kV FEG. FTIR spectra were recorded on a Perkin-Elmer Spectrum One FTIR spectrometer on nanocrystal thin films drop-cast onto a universal ATR sampling accessory. Fixed volumes of a 15 mg/mL suspension of oleate-passivated and pyridine-treated nanocrystals were deposited to allow a comparison of the integrated COO⁻ stretch intensities. Nanocrystal/polymer blends were prepared by blending either pyridine-treated or oleate-passivated PbSe nanocrystals with poly[2-methoxy-5-(3′,7′-dimethyloctyloxy)-p-phenylenevinylene] (MDMO-PPV) dissolved in chlorobenzene at ratios ranging from 0 to 90 wt %. Thin (60−80 nm) films were prepared by spin-casting the blends on either glass or quartz substrates. Absorption spectra were collected with a Perkin-Elmer Lambda 900 spectrophotometer. Photoluminescence
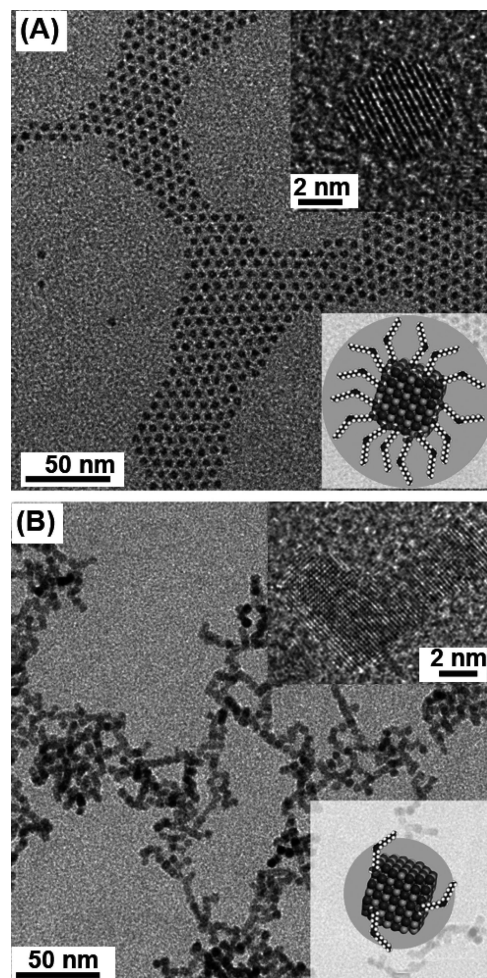

FIGURE 1. TEM images of 4 nm PbSe nanocrystals before (A) and after (B) ligand displacement with pyridine. The insets on the upper right show high-resolution images of isolated and aggregated nanocrystals, respectively. The insets on the lower right provide schematic representations of the nanocrystal and the surrounding zone shielded by the surface ligand.

(PL) spectra of thin-film nanocrystal/polymer blends were acquired with an Edinburgh Instruments FS920 spectrophotometer. PL spectra of PbSe nanocrystal films deposited on n-doped InP substrates were obtained using an Nd:YAG laser operating at 532 nm as an excitation source and a cooled InGaAs linear photodiode array to detect the PL signal.

RESULTS AND DISCUSSION

The TEM images in Figure 1 illustrate the drastic changes in nanostructure morphology that accompany the pyridine treatment. Oleate-capped PbSe nanocrystals with a 4 nm mean diameter condensed into a hexagonal lattice whose interparticle spacing was stabilized by the long oleate chains. When the nanocrystals in Figure 1A were subjected to a single round of pyridine treatment, the nanostructure morphology changed from the well-ordered array of isolated particles to the anisotropic network structure shown in Figure 1B. The high-resolution TEM images in the upper insets of Figure 1 show the shape evolution of individual nanocrystals from initial quasi-spherical oleate-capped nanocrystals to interconnected anisotropic pyridine-treated nanocrystals. The schematics in the lower inset illustrate the
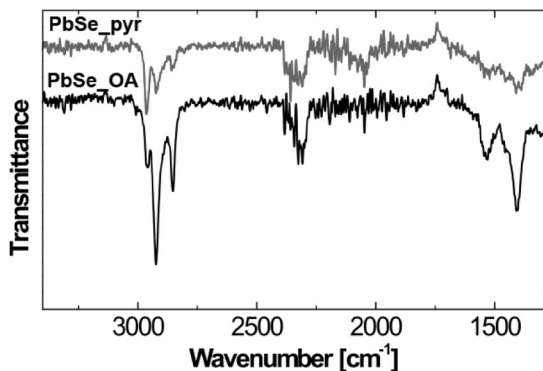
FIGURE 2. FTIR spectra of oleate-capped (PbSe_OA) and pyridine-treated (PbSe_pyr) nanocrystals.

pronounced differences in the stabilization of the initial oleate-capped nanocrystals and the deprotected nanocrystals formed during the pyridine treatment. In oleate-passivated nanocrystals, interparticle attractive forces are balanced by the steric repulsion between the long alkyl chains. In contrast, the deprotected surfaces formed during the pyridine treatment are unable to counterbalance the attractive forces, leading to irreversible assembly of nanocrystals into aggregates and sparse networks (28).

The pyridine treatment strongly influenced the nanocrystals solubility characteristics. Oleate-capped PbSe nanocrystals are readily dispersed in hexane, whereas pyridine-treated nanocrystals are insoluble in hexane. This solubility difference points to a clear modification of the nanocrystal surface chemistry; however, a simple exchange of surface-bound oleate by pyridine does not accurately reflect the underlying mechanism. FTIR spectra fail to show a clear signature of surface-bound pyridine but, rather, suggest a partial displacement, or removal, of oleate groups from the nanocrystal surface, as monitored by the reduced intensity of COO^- stretch intensity near 1500 cm^{-1} (Figure 2). Recent work by Nozik and co-workers (25) on PbSe nanocrystal thin films has confirmed that chemical treatments with various amines, including pyridine, lead to an apparent reduction in surface density of oleate passivants instead of an exchange with amines.

We performed high-resolution TEM analysis of the anisotropic pyridine-treated PbSe nanostructures to gain a better understanding of the interface and crystallography of individual nanocrystals. Figure 3 shows HRTEM images of PbSe nanocrystals subjected to two rounds of pyridine treatment. The images reveal that the anisotropic structures are not comprised of merely aligned nanocrystals but actually formed a crystallographically continuous structure. We stress that such nanocrystal network structures present a desirable morphology for charge transport in photovoltaic applications, since the epitaxially connected particles provide much more efficient charge transport channels compared to interparticle hopping limited charge transport in films of isolated nanocrystals (23, 24). Moreover, nanostructure dimensionalty is expected to significantly influence the recombination dynamics of photogenerated charges (29). In particular, the comparison of MEG efficiency in 1D vs 0D
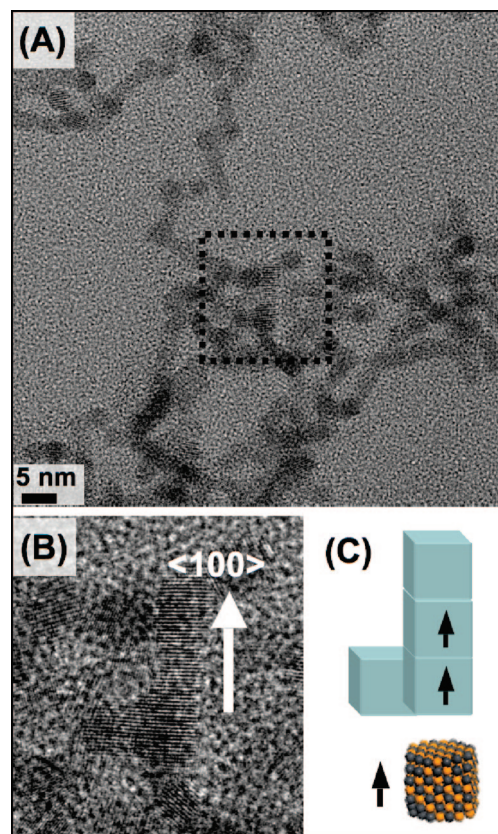

FIGURE 3. High-resolution TEM images of pyridine-treated 4 nm PbSe nanocrystal aggregates, subjected to two rounds of pyridine treatment: (A) crystallographically connected network of pyridine-treated PbSe nanocrystals; (B) high-resolution image from the dashed area in (A), showing the L-shaped nanocrystal cluster. (C) Schematic representation of an L-shaped cluster and the dipole in individual nanocrystals.

nanostructures presents an intriguing yet, to the best of our knowledge, unresolved question.

The high-resolution TEM image (Figure 3A) with {100} lattice planes resolved shows an L-shaped nanocrystal complex that is elongated along the ⟨100⟩ axis. The structure was most likely formed from the fusion of approximately four individual pyridine-treated PbSe nanocrystals, as schematically shown in Figure 3B. Similar dipole-driven oriented attachment and fusion has previously been observed in CdTe nanocrystals subjected to ligand displacement at room temperature (30) and in PbSe nanocrystal suspensions heated to 150 °C (31). Cho et al. (12) later showed that similar dipole-driven assembly processes also occur in seemingly symmetric PbSe nanocrystals. Their work demonstrated that the addition of amine ligands and adjustments under synthesis conditions led to the formation of an impressive spectrum of crystal shapes, including nanowires, star-shaped nanowires, stars, and rings. The formation of these highly anisotropic nanowires from initially quasi-spherical nanocrystal building blocks was attributed to the presence of net dipole moments within individual nanocrystals.

In PbSe nanocrystals such dipoles are believed to arise from the uneven distribution of Pb- and Se-terminated {111} facets, which results in a net dipole along the ⟨100⟩

axis (12). The elongation along the ⟨100⟩ axis in the aniso-tropic structures investigated in this work strongly suggests that these structures formed by a similar dipole directed mechanism. A cryo-TEM study by Klokkenburg et al. (32) showed that, depending on particle concentration and size, the nanocrystal dipoles are sufficiently strong to form similar aligned (but not fused) assemblies of oleate-capped PbSe nanocrystals in solution. These observations suggest that the oleic capping provides sufficient protection to prevent fusion of the nanocrystals while still allowing dipole-mediated nanocrystal alignment, in correspondence with our observations. Vanmaekelbergh, Zandbergen, and co-workers recently reported in situ TEM experiments which showed that amine-passivated PbSe nanocrystals fused along their common ⟨100⟩ axis when annealed at temperatures above 100 °C (33). Their study revealed a number of complex crystallographic processes underlying the crystallographic fusion at formation of defect-free nanocrystal junctions at temperatures far below the PbSe melting point.

To gain more insight into the role of dipoles on nanocrystal network formation, we compared the morphology changes in small (4 nm; quasi-spherical) and large (8 nm; quasi-cubic) nanocrystals subjected to the same pyridine ligand displacement conditions. The TEM images in Figure 4 show that the anisotropic assemblies formed in small PbSe nanocrystals result in crystallographically fused complexes. In contrast, the larger, quasi-cubic nanocrystals were found to form complexes aligned along their ⟨100⟩ axis but importantly maintained their individual nanocrystal character.

The defect-free, epitaxial fusion of {100} facets of small neighboring particles at moderate temperatures (60 °C) points to the high reactivity of {100} facets. However, to explain the diameter-dependent differences in nanostructure assembly, we need to look beyond the relative reactivity of {111} and {100} facets. PbSe nanocrystals are known to undergo shape evolution from quasi-spherical to cubic with increasing nanocrystal size (9, 14, 34). On the basis of the model introduced by Cho et al. (12) the strength of the nanocrystal dipole is therefore the product of the net charge, proportional to the ratio of {111}/{100} facets, and the separation between {111}$_{Pb}$ and {111}$_{Se}$ facets. We calculated the diameter- and shape-dependent dipole interaction strength and found that dipole interactions along the ⟨100⟩ axis are more than 60% weaker in 8 nm particles than in smaller (4 nm) particles (see the Supporting Information). In combination with our experimental observation, this trend demonstrates that the size of nanocrystals allows tuning the complementary and antagonistic interactions that drive the self-assembly of these particles into larger architectures.

The PbSe nanowires formed by Cho et al. (12) were assembled from individual nanocrystals at temperatures exceeding 190 °C. We hence expected pyridine ligand displacement conditions at elevated temperatures, limited by the boiling point of pyridine (115 °C), to favor the formation of similar high aspect ratio anisotropic assemblies. Unfortunately, ligand displacement carried out at temperatures exceeding 70 °C degraded the nanocrystals and
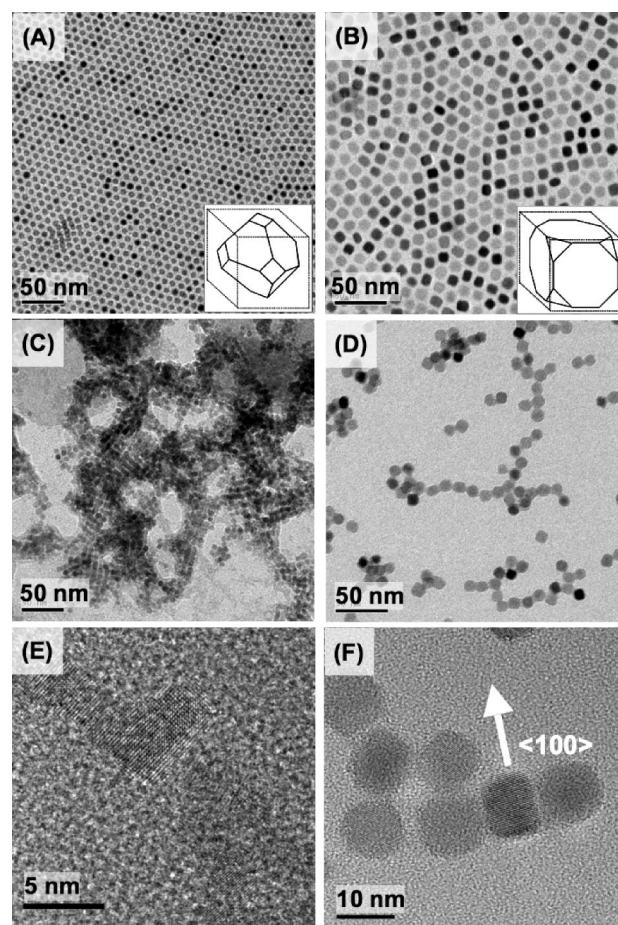

FIGURE 4. TEM images of small (4 nm) and large (8 nm) PbSe nanocrystals subjected to identical pyridine displacement conditions. Before pyridine displacement both samples form well-defined isolated assemblies (A, B). Small PbSe nanocrystals formed crystallographically fused clusters (C, E). Large PbSe nanocrystals form one-dimensional assemblies composed of isolated nanocrystals (D, F). The insets show schematic representations of a small particle (A) with small {100} and large {111} surfaces and a large particle (B) with large {100} and small {111} surfaces.

formed micrometer-sized PbSe crystals. Presumably this treatment completely deprotected the nanocrystal surface. Conversely, pyridine treatment carried out at lower temperatures (20 °C, overnight) did not result in appreciable ligand displacement, as evidenced by the lack of a precipitate upon addition of hexane antisolvent (35). Other control experiments showed that, in the absence of pyridine, 6 nm PbSe nanocrystals stirred in toluene at 60 °C overnight did not undergo dipole-induced morphology changes (see the Supporting Information).

Aside from the strong influence on nanocrystal morphology illustrated above, the nanocrystal surface chemistry is also known to play a critical role in determining the materials optical and electronic properties. For instance, due to the high surface to bulk ratio and the extreme spatial confinement the fate of photogenerated carriers in nanocrystals is critically sensitive to their interaction with the surface ligand. We investigated the influence of pyridine displacement on the optical properties of individual nanocrystals and nanocrystal/polymer blends. Figure 5 illustrates the changes in the optical properties of 4 nm PbSe nanocrystals before and
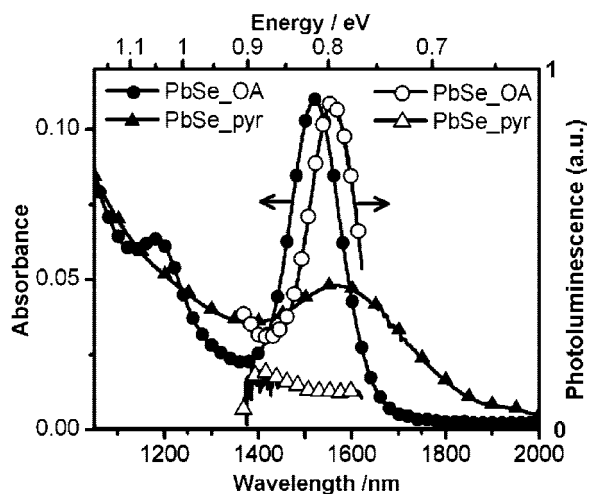
FIGURE 5. Absorption and photoluminescence spectra of oleate-capped (●, ○) and pyridine treated (▲, △) PbSe nanocrystals (diameter 4.2 nm). Absorption measurements were done in solution, and PL measurements were done on nanocrystal films deposited on InP substrates.

after pyridine treatment. The absorption spectrum of oleate-capped nanocrystals showed a well-defined exciton peak with a maximum at 1520 nm (0.815 eV) with a full width at half-maximum (fwhm) of 70 meV. When these nanocrystals were subjected to two pyridine treatment runs, the exciton peak shifted to 1569 nm (0.790 eV) and broadened substantially (fwhm = 160 meV). The red shift of the exciton peak in the networked PbSe nanocrystals is likely the result of the partially relaxed spatial (i.e., quantum) confinement and an increase in midgap surface states. The peak broadening can be attributed to the increase in the nanocrystal size polydispersity and the additional wave function distortion stemming from the influence of surface charges (25). These observations are consistent with trends expected for the transition from zero- to one-dimensional quantum confinement in nanostructures with cubic crystal structure (36). In contrast, one-dimensional CdSe nanorods and tetrapods show no length-dependent absorbance trends (37, 38). In the case of one-dimensional CdSe nanostructures, the intrinsically asymmetric hexagonal crystal structure gives rise to strong quantum confinement in the radial direction, but not along the elongated axis (39). The possibility of partially oxidizing the pyridine-treated PbSe nanocrystal suspension during measurement can be excluded, since the oxidation of the nanocrystal surface would result in a blue shift of the exciton peak (40). Importantly, our optical measurements confirm the preservation of size-dependent optical properties in our confined-but-connected PbSe nanocrystal network structures.

Figure 5 also shows photoluminescence (PL) spectra of oleate-capped and pyridine-treated nanocrystal thin films on InP substrates. The oleate-capped nanocrystals showed a clear exciton PL peak at 1560 nm (0.795 eV). The 20 meV red shift of the excitonic PL in the oleate-capped film relative to the absorbance peak measured in solution is primarily due to the Stokes shift. Enhanced electronic coupling and energy transfer between the particles in the film compared to those in solution are also expected to contribute to the red shift
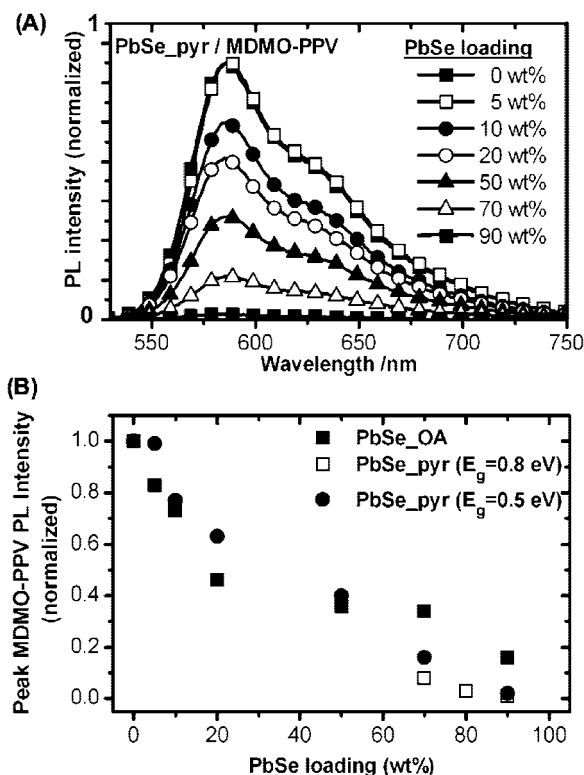

FIGURE 6. Photoluminescence measurements of PbSe/MDMO-PPV blends: (A) PL spectra of blends with varying PbSe concentration; (B) PL quenching by oleate-capped (■; 4 nm) and pyridine-treated (□, ●; 4 and 9 nm, respectively) nanocrystals.

(41). Significantly, previous studies of oleate-capped PbSe nanocrystals by Du et al. (8) have shown quantum yields as high as 81% in the absence of any inorganic passivating shell. Such a shell is usually required to attain quantum yields similar to those in other semiconductor materials (42, 43). These spectroscopic studies further support that oleate-capped PbSe nanocrystals have a relatively low density of optically active surface states. We did not detect any significant nanocrystal PL in our measurements of pyridine-treated PbSe nanocrystal thin films (Figure 5). The PL quenching is likely due to the high density of optically active surface defects introduced by the pyridine treatment, although further experiments are needed to elucidate the complex relation between nanocrystal photoluminescence and the physical and chemical surface properties.

Finally, we investigated the influence of nanocrystal surface chemistry on the optical properties of blends of oleate-capped or pyridine-treated nanocrystals and a conjugated polymer (MDMO-PPV). Figure 6A shows PL spectra of pyridine-treated PbSe nanocrystal/MDMO-PPV blends, excited at 530 nm, at nanocrystal loadings ranging from 0 to 90 wt %. In blends comprised of 90 wt % (∼ 50 vol %) of PbSe in MDMO-PPV, approximately 98% of the polymer PL was quenched. Figure 6B compares the PL intensity of blends made from the polymer with oleate-capped or pyridine-treated PbSe with that of pristine MDMO-PPV. In contrast to the work on CdSe/PPV blends by Greenham et al. (44), we found that the extent of PL quenching was relatively insensitive to the nanocrystal surface chemistry. We further investigated the influence of the nanocrystal

band gap by blending PbSe nanocrystals with different diameters (4 nm, $E_g = 0.8$ eV; 9 nm, $E_g = 0.5$ eV) and found no significant trend with the nanocrystal band gap, in accord with optical studies of CdSe/PPV blends and device studies of PbSe/PPV blends (7).

The PL quenching in these polymer/nanocrystal (i.e., donor/acceptor) blends is due to two competing mechanisms: charge transfer and resonance energy transfer. The former process is desired for photovoltaic applications, since it facilitates exciton dissociation. Charge transfer relies on direct donor/acceptor (D/A) wave function overlap and is hence strongly influenced by the D/A separation (i.e., capping ligand length) and D/A energy level alignment. Energy transfer, on the other hand, relies on Coulomb interaction and is much less impaired by the presence of capping layer on the nanocrystal surface (45). The weak influence of nanocrystal surface chemistry and band gap observed in the PbSe/polymer blends investigated in this study therefore suggests that the PL quenching is predominantly due to energy transfer. We have performed PL lifetime and temperature-dependent photoinduced absorption measurements of PbSe/PPV and PbSe/P3HT blends to gain a better understanding of the energy and charge transfer mechanisms. These preliminary studies showed optical signatures of short-lived polarons on the polymer chain, suggesting that at least part of that PL quenching can be ascribed to interfacial charge transfer. This will be subject of further investigations.

CONCLUSION

In conclusion, we have shown that pyridine ligand displacement strongly influenced the morphology and assembly of PbSe nanocrystals. The oleic acid ligand provided a robust passivation of the nanocrystal surface and counterbalanced interparticle attractive forces to prevent aggregation. Pyridine treatment leads to a partially deprotected nanocrystal surface that is unable to screen interparticle attractions and, in the case of small nanocrystals, led to the formation of a crystallographically interconnected nanocrystal network. In contrast, larger, nearly cubic nanocrystals aligned into anisotropic assemblies without crystallographic fusion. Optical characterization revealed a red shift and broadening of the exciton absorption peak in pyridine-treated PbSe nanocrystals relative to the oleate-passivated starting material. The PL in the original oleate-capped nanocrystals was completely absent in pyridine-treated samples. PL quenching measurements of PbSe/MDMO-PPV blends showed that the interactions between the nanocrystal and polymer were largely insensitive to the surface chemistry or the band gap of the nanocrystals, suggesting that most of the observed quenching is the result of energy rather than charge transfer. This work underlines the critical role of nanocrystal surface chemistry in obtaining the morphologies and interface transport characteristics required for nanocrystals in photovoltaic devices.

Supporting Information Available: Text and figures giving calculations of the diameter-dependent strength of the nanocrystal dipole and TEM images of a control experiment demonstrating the absence of structural changes when a PbSe nanocrystal suspension was heated in toluene. This material is available free of charge via the Internet at http://pubs.acs.org.

REFERENCES AND NOTES

(1) Huynh, W. U.; Peng, X. G.; Alivisatos, A. P. *Adv. Mater.* **1999**, *11*, 923–927.

(2) Milliron, D. J.; Gur, I.; Alivisatos, A. P. *MRS Bull.* **2005**, *30*, 41–44.

(3) Huynh, W. U.; Dittmer, J. J.; Alivisatos, A. P. *Science* **2002**, *295*, 2425.

(4) Sun, B. Q.; Snaith, H. J.; Dhoot, A. S.; Westenhoff, S.; Greenham, N. C. *J. Appl. Phys.* **2005**, *97*, 014914.

(5) Wang, P.; Abrusci, A.; Wong, H. M. P.; Svensson, M.; Andersson, M. R.; Greenham, N. C. *Nano Lett.* **2006**, *6*, 1789–1793.

(6) Efros, A. L.; Efros, A. L. *Sov. Phys. Semicond.* **1982**, *16*, 772–779.

(7) Jiang, X. M.; Schaller, R. D.; Lee, S. B.; Pietryga, J. M.; Klimov, V. I.; Zakhidov, A. A. *J. Mater. Res.* **2007**, *22*, 2204–2210.

(8) Du, H.; Chen, C. L.; Krishnan, R.; Krauss, T. D.; Harbold, J. M.; Wise, F. W.; Thomas, M. G.; Silcox, J. *Nano Lett.* **2002**, *2*, 1321–1324.

(9) Pietryga, J. M.; Schaller, R. D.; Werder, D.; Stewart, M. H.; Klimov, V. I.; Hollingsworth, J. A. *J. Am. Chem. Soc.* **2004**, *126*, 11752–11753.

(10) Cui, D.; Xu, J.; Zhu, T.; Paradee, G.; Ashok, S. *Appl. Phys. Lett.* **2006**, *88*, 183111.

(11) Luther, J. M.; Law, M.; Beard, M. C.; Song, Q.; Reese, M. O.; Ellingson, R. J.; Nozik, A. J. *Nano Lett.* **2008**, *8*, 3488–3492.

(12) Cho, K.-S.; Talapin, D. V.; Gaschler, W.; Murray, C. B. *J. Am. Chem. Soc.* **2005**, *127*, 7140–7147.

(13) Houtepen, A. J.; Koole, R.; Vanmaekelbergh, D. L.; Meeldijk, J.; Hickey, S. G. *J. Am. Chem. Soc.* **2006**, *128*, 6792–6793.

(14) Lu, W.; Fang, J.; Ding, Y.; Wang, Z. L. *J. Phys. Chem. B* **2005**, *109*, 19219–19222.

(15) Schaller, R. D.; Klimov, V. I. *Phys. Rev. Lett.* **2004**, *92*, 186601/1–186601/4.

(16) Ellingson, R. J.; Beard, M. C.; Johnson, J. C.; Yu, P. R.; Micic, O. I.; Nozik, A. J.; Shabaev, A.; Efros, A. L. *Nano Lett.* **2005**, *5*, 865–871.

(17) Luque, A.; Marti, A.; Nozik, A. J. *MRS Bull.* **2007**, *32*, 236–241.

(18) Trinh, M. T.; Houtepen, A. J.; Schins, J. M.; Hanrath, T.; Piris, J.; Knulst, W.; Goossens, A. P. L. M.; Siebbeles, L. D. A. *Nano Lett.* **2008**, *8*, 1713–1718.

(19) Shockley, W.; Queisser, H. J. *J. Appl. Phys.* **1961**, *32*, 510–519.

(20) Klimov, V. I. *Appl. Phys. Lett.* **2006**, *89*, 123118.

(21) Hanna, M. C.; Nozik, A. J. *J. Appl. Phys.* **2006**, *100*, 074510/1–074510/8.

(22) Liu, J. S.; Tanaka, T.; Sivula, K.; Alivisatos, A. P.; Frechet, J. M. J. *J. Am. Chem. Soc.* **2004**, *126*, 6550–6551.

(23) Talapin, D. V.; Murray, C. B. *Science* **2005**, *310*, 86–89.

(24) Murphy, J. E.; Beard, M. C.; Nozik, A. J. *J. Phys. Chem. B* **2006**, *110*, 25455–25461.

(25) Law, M.; Luther, J. M.; Song, O.; Hughes, B. K.; Perkins, C. L.; Nozik, A. J. *J. Am. Chem. Soc.* **2008**, *130*, 5974–5985.

(26) Yu, W. W.; Falkner, J. C.; Shih, B. S.; Colvin, V. L. *Chem. Mater.* **2004**, *16*, 3318–3322.

(27) Murray, C. B.; Norris, D. J.; Bawendi, M. G. *J. Am. Chem. Soc.* **1993**, *115*, 8706–8715.

(28) Mattoussi, H.; Cumming, A. W.; Murray, C. B.; Bawendi, M. G.; Ober, R. *Phys. Rev. B: Condens. Matter* **1998**, *58*, 7850–7863.

(29) Htoon, H.; Hollingsworth, J. A.; Dickerson, R.; Klimov, V. I. *Phys. Rev. Lett.* **2003**, *91*, 227401/1–227401/4.

(30) Tang, Z.; Kotov, N. A.; Giersig, M. *Science* **2002**, *297*, 237.

(31) Sashchiuk, A.; Amirav, L.; Bashouti, M.; Krueger, M.; Sivan, U.; Lifshitz, E. *Nano Lett.* **2004**, *4*, 159–165.

(32) Klokkenburg, M.; Houtepen, A. J.; Koole, R.; de Folter, J. W. J.; Erne, B. H.; van Faassen, E.; Vanmaekelbergh, D. *Nano Lett.* **2007**, *7*, 2931–2936.

(33) van Huis, M. A.; Kunneman, L. T.; Overgaag, K.; Xu, Q.; Pandraud, G.; Zandbergen, H. W.; Vanmaekelbergh, D. *Nano Lett.* **2008**, *8*, 3959–3963.

(34) Lee, S.-M.; Jun, Y.-W.; Cho, S.-N.; Cheon, J. *J. Am. Chem. Soc.* **2002**, *124*, 11244–11245.

(35) Efforts to accomplish pyridine ligand displacement by sonicating the nanocrystal/pyridine suspension for extended periods of time at room temperature were unsuccessful. While this approach allows a partial ligand removal, a consistent trend could not be developed. We attribute this inconsistency to the variability associated with the presence of local hot spots within the sonication bath.

(36) Kan, S. H.; Aharoni, A.; Mokari, T.; Banin, U. *Faraday Discuss.* **2004**, *125*, 23–38.

(37) Manna, L.; Milliron, D. J.; Meisel, A.; Scher, E. C.; Alivisatos, A. P. *Nat. Mater.* **2003**, *2*, 382–385.

(38) Li, L.; Hu, J. T.; Yang, W. D.; Alivisatos, A. P. *Nano Lett.* **2001**, *1*, 349–351.

(39) Efros, A. L.; Rosen, M. *Annu. Rev. Mater. Res.* **2000**, *30*, 475–521.

(40) Stouwdam, J. W.; Shan, J.; van Veggel, F.; Pattantyus-Abraham, A. G.; Young, J. F.; Raudsepp, M. *J. Phys. Chem. C* **2007**, *111*, 1086–1092.

(41) Luther, J. M.; Beard, M. C.; Song, Q.; Law, M.; Ellingson, R. J.; Nozik, A. J. *Nano Lett.* **2007**, *7*, 1779–1784.

(42) Hines, M. A.; Guyot-Sionnest, P. *J. Phys. Chem.* **1996**, *100*, 468.

(43) Peng, X.; Schlamp, M. C.; Kadavanich, A. V.; Alivisatos, A. P. *J. Am. Chem. Soc.* **1997**, *119*, 7019–7029.

(44) Greenham, N. C.; Peng, X. G.; Alivisatos, A. P. *Synth. Met.* **1997**, *84*, 545–546.

(45) Achermann, M.; Petruska, M. A.; Kos, S.; Smith, D. L.; Koleske, D. D.; Klimov, V. I. *Nature* **2004**, *429*, 642–646.